Solubility of niobium(V) in cementitious systems relevant for nuclear waste disposal: Characterization of the solubility-controlling solid phases

Yongheum Jo [a,*], Krassimir Garbev [b], Neşe Çevirim-Papaioannou [a], Oliver Dieste Blanco [a], Benny de Blochouse [c], Marcus Altmaier [a], Xavier Gaona [a,*]

[a] Institute for Nuclear Waste Disposal, Karlsruhe Institute of Technology, Karlsruhe, Germany
[b] Institute for Technical Chemistry, Karlsruhe Institute of Technology, Karlsruhe, Germany
[c] ONDRAF/NIRAS, Sint-Joost-ten-Node, Belgium

GRAPHICAL ABSTRACT

- Sparingly soluble calcium niobium oxides identified in cementitious pore water.
- Formation of ternary complexes Ca-Nb(V)-OH(aq) proposed in alkaline systems.
- Cubic pyrochlore, $Ca_2Nb_2O_7$(s), controls Nb(V) solubility at pH > 12 and [Ca] ≥ 30 mM.
- Solubility-control by columbite, $CaNb_2O_6$(cr) favored at lower pH and [Ca].
- Key input to estimate the solubility control of ^{94}Nb in repositories for nuclear waste.

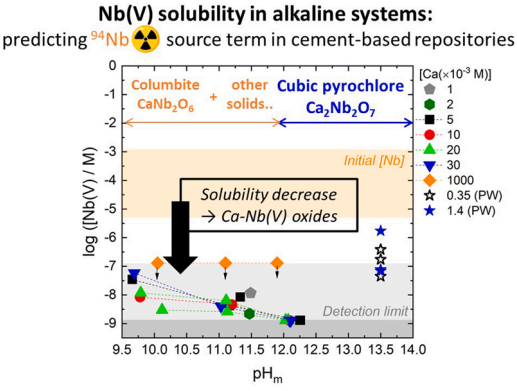

ABSTRACT

Editor: Sungjun Bae

Keywords:
Niobium
Solubility
Cement
Solid characterization
Radioactive waste disposal

Neutron activation of ^{93}Nb in structural materials of nuclear reactors generates the radioactive, $\beta^-\gamma$ emitting ^{94}Nb isotope ($t_{1/2}$= $2.04 \cdot 10^4$ a). Waste streams containing ^{94}Nb are disposed in repositories for low- and intermediate-level waste, which are characterized by the extensive use of cementitious materials. The chemical behavior of niobium in these systems remains ill-defined, especially with respect to the solid phases controlling its solubility. Oversaturation solubility experiments in synthetic solutions representative of cementitious pore water ($10 \leq pH \leq 12.5$) show the precipitation of Nb, with [Nb] < 10^{-7} M at equilibrium. The increase in solubility observed at pH > 12.5 is attributed to negatively charged hydrolysis species stabilized by Ca. Solids controlling Nb solubility were characterized by a multi-method approach. XRD, Raman and quantitative chemical analysis support the predominance of cubic pyrochlore $Ca_2Nb_2O_7$(cr) at pH ≈ 13.5, as well as in systems at pH ≈ 12 and high [Ca]. The incorporation of K in the pyrochlore structure was observed in pore water systems containing potassium, whereas $CaNb_2O_6$(cr) plays a predominant role at pH ≈ 10–11. This work provides an improved scientific basis to assess solid phase formation and solubility behavior of Nb(V) in cementitious systems relevant for nuclear waste disposal.

* Corresponding authors.
E-mail addresses: yongheum.jo@kit.edu (Y. Jo), xavier.gaona@kit.edu (X. Gaona).

1. Introduction

Niobium (Nb) is a transition metal widely used in the manufacturing of special alloys and high strength steels (Collier et al., 1988; Wang et al., 2009), which receive increasing attention in a range of applications such as energy storage (Zhang et al., 2019), electrocatalyst (Li et al., 2014), photocatalyst (Zhou et al., 2020), and piezoelectric sensor (Brandon and Megaw, 1970). In nuclear power reactors, neutron activation of stable ^{93}Nb present in structural materials (e.g., Ni-based alloys, stainless steel) generates the radioactive isotope ^{94}Nb, which is characterized by β^- γ emission and a half-life of $t_{1/2}$ $2.04{\cdot}10^4$ a (Schuman and Goris, 1959; He et al., 2012). ^{94}Nb generated during the operation of the nuclear reactor considerably contributes to the activity of waste streams arising from the coolant treatment and the dismantlement of the nuclear reactor, which are normally disposed of in repositories for low- and intermediate-level radioactive waste (L/ILW) (Wang et al., 2009; Adams and Carboneau, 1995; Espartero et al., 1998). ^{94}Nb is classified within the high radiotoxicity group uniformly affecting the whole-body rather than focusing on a certain organ (Adams and Carboneau, 1995).

Cementitious materials (cement, concrete, mortar, and grout) are extensively used in repositories for L/ILW for the stabilization of the waste and for construction purposes. In the event of formation water interacting with cementitious materials, pore water solutions characterized by (highly) alkaline pH conditions will form. Cement degradation caused by the interaction with groundwater is generally described by three subsequent degradation stages, I to III. Pore water of fresh cement in the degradation stage I is dominated by the dissolution of Na_2O and K_2O, which buffer the pH above $\approx$ 13 and sets relatively low Ca concentrations, i.e., [Ca] $< 10^{-3}$ M. After the washing out of the alkali oxides, the pore water composition is controlled by the equilibrium with portlandite, $Ca(OH)_2$(cr), at pH $\approx$ 12.5 and [Ca] $\approx 2 \times 10^{-2}$ M (degradation stage II). The final degradation stage (III) involves the incongruent dissolution of calcium silicate hydrate (C-S-H) phases with 10 $\leq$ pH $\leq$ 12.5 and 10^{-4} M $\leq$ [Ca] $\leq 10^{-2}$ M. In the context of waste disposal in rock salt formations, the corrosion of hardened cement paste (HCP) by $MgCl_2$-dominated brines was shown to result in high $CaCl_2$ concentrations (2–4 M) in combination with high pH values ($pH_m \approx 12$, with pH_m –log [H^+]) under specific conditions (Bube et al., 2013).

Nb is predominantly found in the pentavalent oxidation state within the stability field of water and is the only relevant oxidation state under the conditions of this study. Nb(V) forms sparingly soluble oxides and is characterized by an amphoteric behavior, involving the formation of cationic and anionic hydrolysis species below and above pH $\approx$ 4, respectively (Peiffert et al., 2010). In alkaline systems containing Na, the increase in the solubility of β-Nb_2O_5(cr) caused by the predominance of the anionic species $Nb(OH)_6^-$ and $Nb(OH)_7^{2-}$ leads to the formation of highly soluble ternary solid phases (e.g., $Na_8Nb_6O_{19}{\cdot}13$ H_2O(cr), $Na_7HNb_6O_{19}{\cdot}15$ H_2O(cr), with [Nb] $> 1 \times 10^{-3}$ M) at pH > 9 (Peiffert et al., 2010; Deblonde et al., 2015a). Under these conditions, polyniobiate ions dominate the aqueous speciation of Nb(V), expectedly stabilized by the formation of ion-pairs with alkali ions present in solution (Nyman, 2011; Deblonde et al., 2015b).

In alkaline systems containing Ca, several studies have confirmed a significant decrease in the Nb solubility (with $[Nb]_{eq} \approx 10^{-9}$–$10^{-5}$ M, depending upon pH and [Ca]), which is attributed to the formation of sparingly soluble ternary solid phases of the type Ca-Nb(V)-O/OH(s) (Pilkington and Stone, 1990; Lothenbach et al., 1999; Talerico et al., 2004; Pointeau et al., 2004; Yamaguchi et al., 2020; Tachi et al., 2020; Çevirim-Papaioannou et al., 2022). However, the stoichiometry and structure of these solid phases remain ill-defined, and a variety of compounds have been proposed to control the solubility of Nb(V) in cementitious environments, e.g., $CaNb_2O_6{\cdot}nH_2O$(s) (Lothenbach et al., 1999), $CaNb_4O_{11}{\cdot}8$ H_2O(cr) (hochelagaite) (Talerico et al., 2004), Ca $(NbO_3)_2$(s) (Yamaguchi et al., 2020) or pyrochlore-type $Ca_2Nb_2O_7$(cr) (Çevirim-Papaioannou et al., 2022). We note that pyrochlore ((Na,Ca, Ce)$_2$(Nb,Ti,Ta)$_2$(O,OH,F)$_7$) and columbite ((Fe,Mn)(Nb,Ta)$_2$O$_6$) are the principal ore minerals of niobium, although a number of other mineral groups are also described in the literature, e.g., perovskite, rutile, among others (Gasik, 2013; Schulz et al., 2017).

In this context, this work aims at systematically investigating the solubility of Nb(V) under conditions relevant for cement-based repositories for nuclear waste disposal, i.e., with 10 $\leq$ pH $\leq$ 13.5 and $3.5{\times}10^{-4}$ M $\leq$ [Ca] $\leq 3{\times}10^{-2}$ M. Additional solubility experiments in alkaline 1 M $CaCl_2$ solutions give insight on the behavior of Nb solubility in cementitious systems potentially exposed to brine solutions. Special focus is given to the identification of the solid phases controlling the solubility of Nb in these systems, for which a multi-method approach involving X-ray diffraction (XRD), scanning electron microscopy with energy dispersive spectroscopy (SEM-EDS), Raman spectroscopy, thermogravimetric (TG) analysis and quantitative chemical analysis is used.

2. Experimental

2.1. Chemicals and materials

All solutions were prepared with purified water (Milli—Q academic, Millipore, 18.2 MΩ·cm) purged with Ar for $\approx$ 3 h. $Ca(OH)_2$, Na_2SO_4, $CaCO_3$, $CaCl_2{\cdot}2$ H_2O (EMSURE®), HNO_3 (60%, Ultrapur), HF (48%, Ultrapur), HCl, KOH, and NaOH (Titrisol®) were obtained from Merck and used without further purification. $NbCl_5$ (99%) was purchased from Sigma-Aldrich. Cement CEM I 52,5 N SR0 CE PM-CP2 NF provided from ONDRAF/NIRAS was hydrated with a water-to-cement ratio of 0.46. After 2.5 months hydration, the outer surface ($\approx$ 2.5 mm) of the hardened cement paste (HCP) monolith was removed by circular saw to avoid any possible surface alteration. The remaining material was crushed, milled, and sieved to $<$ 63 μm as described in (Cachoir et al., 2006). Young cement pore water (YCWCa) was prepared following the protocol developed by SCK·CEN (Cachoir et al., 2006). Briefly, targeted volumes / amounts of 1.0 M NaOH, 1.0 M KOH, Na_2SO_4(s), $CaCO_3$(s), Ca $(OH)_2$(s), and purified water were mixed in volumetric flasks to obtain the following composition: [Na] 0.14 M, [K] 0.37 M, [Ca] $3.5{\cdot}10^{-4}$ M, [SO_4^{2-}] $2{\cdot}10^{-3}$ M, and [CO_3^{2-}] $3{\cdot}10^{-4}$ M at pH $\approx$ 13.5. The contact of this artificial pore water with the HCP powder resulted in a slight increase in Ca concentration to $1.4{\cdot}10^{-3}$ M, which was accordingly corrected in the final YCWCa recipe. The concentration of other metal ions remained the same as in the initial YCWCa. The chemical composition of the cement pore water was characterized by inductively coupled plasma atomic emission spectroscopy (ICP-OES) after 0.1 μm membrane filtration (Durapore®).

2.2. pH measurements

The experimental pH (pH_{exp}) was measured using combination pH electrodes (ROSS Orion) calibrated by linear regression against standard pH buffers (pH 9.0–12.0, Merck). The recorded potential (mV) by pH meter (Orion Star™ A211 Benchtop) was converted to pH value. For the samples in 1.0 M $CaCl_2$, the molal H^+ concentration (m_{H+}) was determined by correcting the measured pH_{exp} with the empirical value A_m (pH_m $pH_{exp} + A_m$, where pH_m $\log m_{H+}$), which entails the activity coefficient of the proton and the contribution of the liquid junction potential of the electrode at this background electrolyte concentration. A value of A_m(1.0 M $CaCl_2$) 0.334 was used based on the previous work by Altmaier and co-workers (Altmaier et al., 2008). In the YCWCa solutions with [NaOH] + [KOH] $\approx$ 0.5 M, the H^+ concentration was calculated from the given [OH^-] and the conditional ion product of water at this ionic strength.

2.3. Nb(V) solubility experiments

All experiments were performed in Ar-gloveboxes (MBRAUN) with $O_2 < 2$ ppm at T (22 ± 2) °C. Nb(V) solubility was investigated from

oversaturation conditions. A 1.3 × 10^{-3} M Nb(V) stock solution was prepared by dissolving the required amount of $NbCl_5$ in 0.02 M NaOH. The dissolution of $NbCl_5$ was complete after ≈ 1 week. A 2.0 M $CaCl_2$ stock solution was prepared by dissolving $CaCl_2{\cdot}2\,H_2O$ in purified water. The Nb(V) stock solutions was added to purified water or YCWCa solutions to obtain the targeted initial concentrations of Nb(V) (5 ×10^{-6} M – 1.2 ×10^{-3} M). The 5 × 10^{-3} M – 3 × 10^{-2} M and 1.0 M Ca concentration was obtained by the addition of Ca stock in purified water. An additional series was prepared by adding $NbCl_5$(s) directly into the Ca-containing solutions, i.e., without a dissolution step in 0.02 M NaOH, but no clear difference between both approaches was observed. A total of 30 batch samples were prepared and stored in Oak Ridge PPCO centrifuge tubes (Nalgene™) with an initial volume of 50 mL. HCl and NaOH solutions were used to adjust the pH_m to ≈ 10, ≈ 11, and ≈ 12. Table 1 summarizes the experimental conditions in the solubility experiments.

The pH and [Nb(V)] in the solubility samples were determined after contact times of t 32, 57, and 200 days. Aliquots of the supernatant solutions were taken, and the aqueous phase was separated by ultrafiltration with 10 kD filters (Nanosep® centrifuge tubes, Pall Life Sciences, ≈ 2 nm cut-size). Before sampling, each filter was washed 3 times with the corresponding sample solution to exclude sorption effects. After phase separation, the filtrate was diluted in 2% HNO_3 and the concentration of Nb(V) in the aqueous phase was quantified by inductively coupled plasma mass spectroscopy (ICP-MS) using a iCAP TQs Thermo Scientific™ equipment. The detection limit of the measurement was calculated as 3 times the standard deviation (3σ) of blank samples (2% ultrapure HNO_3) and considering the corresponding dilution factors.

2.4. Nb(V) solid characterization

Solid phases collected from selected solubility experiments were characterized after attaining equilibrium conditions, which were assumed after subsequent constant pH_m and [Nb(V)] measurements over extended periods of time. An aliquot of each suspension was transferred to a 2 mL polypropylene micro-centrifuge tube and centrifuged for 5 min at 14,000g. The supernatant was discarded and the separated solid was washed with ethanol to remove the matrix solution. The centrifugation and washing steps were repeated 3 times, and the washed solid was characterized after drying under Ar atmosphere. A fraction of the dry solid was completely dissolved in a mixture solution of 1 mL 2% HNO_3 (Suprapur®, Merck) and 21.2 µL 48% HF (Ultrapur, Merck). Note that the dissolution with the sole use of concentrated HNO_3, HCl, or H_2SO_4 was not successful and the addition of HF was required to achieve the complete dissolution of the solid. The composition (K, Na, Ca, and Nb) of solid was determined by ICP-OES (Optima 8300, PerkinElmer) after dilution in 2% HNO_3.

The remaining dry solid was characterized by powder X-ray diffraction (XRD), scanning electron microscopy with energy dispersive spectroscopy (SEM-EDS), Raman spectroscopy, and thermogravimetic (TG) analysis. XRD patterns were collected with a Bruker D8 Advance X-ray powder diffractometer with Cu Kα radiation. Measurements were conducted at 2θ 10 – 90 with 0.013 incremental steps and a measurement time of 1.5 s per step. The SEM used in this work (FEI Quanta 650 FEG) was equipped with secondary electron detector (SE, providing topology information on the sample), backscattered electron detector (BSE, providing Z-related contrast), and energy dispersive X-ray spectroscopy detector (EDS, Thermo Scientific, NORAN System 7). The EDS spectra were obtained and analyzed with the software Pathfinder version 2.8, providing elemental composition with high lateral resolution. The samples were deposited on standard carbon stickers glued to aluminum SEM stabs, with no further preparation. The lack of coating with conductive material (such as Carbon or Gold) led to some charging effect visible on some of the SE images, but negligible on the BSE ones.

Confocal Raman spectroscopic single spot measurements and mappings were performed for samples on Au coated specimen slides. A WITec alpha300 R equipped with UHTS300 spectrometer (300 mm focal length) and Zeiss microscope was used. A 532 nm laser was used as excitation source, which was operated by a TruePower module in the range between 10 and 40 mW (energy depending on the sample stability). Single spot measurements were performed with a 100 × objective with a numerical aperture (NA) of 0.9 using 600 and 1800 gratings (spectral resolution better than 3 cm^{-1} and 1 cm^{-1}, respectively). A high performance back illuminated CCD Camera was used for the detection. Typical acquisition times were between 5 and 10 s with 5 – 10 scans. In addition, 2D Raman mappings with typical areas ranging between 50 × 50 and 100 × 100 µm were performed in 1 µm step. The TrueSurface module combined with objectives 20 × , 50 × and 100 × (NA 0.75, 0.75, and 0.90, respectively) allowed precise focusing on the uneven sample surface and topographic imaging. The phase identification was aided by the RRUFF mineral database (Lafuente et al., 2015) and own database integrated in the WITec TrueMatch program. The data processing performed with the Project 5.3 + software including cosmic ray removal, background subtraction, and preparation of the false color Raman images. The hyperspectral data sets from Raman mappings were analyzed by the module True Component Analysis using basis spectra data sets and residual image analysis.

TG measurements were performed with a STA 449 C (NETZSCH) equipment under 1.8 L/h Ar stream at 25 – 1100 C with incremental rate of 10 C/min. Due to amount of solid required for TG analysis (*ca.* 10 mg), only the sample equilibrated in pore water with [Ca] 1.4 × 10^{-3} M was characterized with this technique.

3. Results and discussion

3.1. Nb(V) solubility

Solubility samples containing $[Nb(V)]_0 > 5{\cdot}10^{-4}$ M started from oversaturation clearly showed the formation of a white solid phase within the first hours after mixing the Nb(V) and Ca stock solutions in alkaline conditions. Fig. 1 shows the concentration of dissolved Nb(V) after 200 days of equilibration time in the alkaline solutions containing Ca at pH_m ≈ 9.5 – 12.5 and cementitious pore water at pH_m ≈ 13.5. No clear trend in the measured concentration of Nb(V) as a function of the equilibration time was observed (see Table SD-1 in Supplementary Data). The solubility lines of β-Nb_2O_5 and $Na_8Nb_6O_{19}{\cdot}13H_2O$(cr) in 0.3 m $NaClO_4$, which would predict much higher concentrations than those actually measured in our study, are plotted for comparison. Solubility calculations were performed using thermodynamic data reported in (Peiffert et al., 1997) and partially selected in the ThermoChimie database (Grivé et al., 2015).

The dissolved Nb(V) concentration noticeably decreased in all samples within the timeframe of the study, i.e., 2–6 log_{10}-units as compared to the initial [Nb(V)]. All samples equilibrated in 1.0 M $CaCl_2$ resulted in [Nb] below the detection limit of the quantification method (≈ 10^{-7} M, considering the strong dilution factor required for these specific samples for ICP-MS). As evidenced in Fig. 1, the observed decrease in the

Table 1
Experimental conditions considered in the Nb(V) solubility experiments in Ca-containing alkaline solutions and cementitious pore water.

Solutions	$[Nb(M)]_0$	Initial pH_m	[Ca(M)]	[Na(M)]	[K(M)]
Alkaline	5.0 × 10^{-6}–1.2 × 10^{-3}	10, 11, 12	5.0 × 10^{-3}–3.0 × 10^{-2}, 1.0	1.5 × 10^{-3}–3.3 × 10^{-2}	–
Cementitious pore water	1.0 × 10^{-5}–1.2 × 10^{-3}	13.5	3.5 × 10^{-4}, 1.4 × 10^{-3}	0.14	0.37

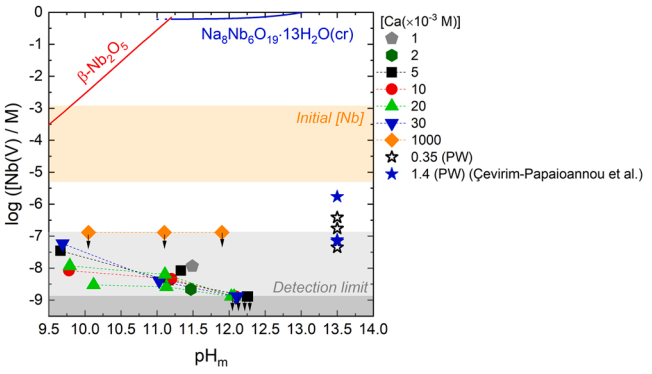

Fig. 1. Nb(V) solubility obtained in the alkaline solutions containing Ca at $pH_m \approx 9.5 - 12.5$ and in cementitious pore water (PW) systems at pH ≈ 13.5. All data corresponding to an equilibration time of 200 days. The solubility lines of β-Nb_2O_5 and $Na_8Nb_6O_{19}$·13 H_2O(cr) were calculated in 0.3 m $NaClO_4$ solution using thermodynamic data partially selected in ThermoChimie (Grivé et al., 2015). Solubility data points obtained for samples with the same initial conditions except pH_m are connected with dashed lines. Note that the dissolved Nb (V) concentrations at $pH_m \approx 12$ or in 1.0 M $CaCl_2$ were below detection limit (down arrow) of $< 1.3 \times 10^{-9}$ M and $< 1.3 \times 10^{-7}$ M, respectively.

concentrations of Nb(V) cannot be explained by a solubility-control of either β-Nb_2O_5 or $Na_8Nb_6O_{19}$·13 H_2O(cr). These results confirm the key role of Ca in defining the solubility of Nb(V) in alkaline to hyperalkaline conditions, as previously suggested in the literature (Lothenbach et al., 1999; Talerico et al., 2004; Yamaguchi et al., 2020). Fig. 1 shows also that, for systems at $pH_m < 12.5$ containing the same [Ca], the concentration of Nb(V) decreases with increasing pH_m, suggesting that pH is also a relevant parameter in the equilibrium reactions controlling the solubility of Nb(V) in cementitious systems. Note that all samples at $pH_m \approx 12–12.5$ show the lowest [Nb(V)] ($< 1.3 \times 10^{-9}$ M, below the detection limit of the quantification method), which is in line with previous observations reported by Lothenbach and co-workers with [Nb(V)] $< 5.4 \times 10^{-8}$ M in solutions containing 0.02 M NaOH and 0.03 M Ca (Lothenbach et al., 1999). Higher concentrations of Nb(V) ($4.5 \times 10^{-8} – 1.7 \times 10^{-6}$ M) are determined in the samples at pH ≈ 13.5 representative of cementitious pore waters in the degradation stage I (see star symbols in Fig. 1), which are also characterized by lower Ca concentrations (3.5×10^{-4} and 1.4×10^{-3} M). For samples containing [Ca] $< 10^{-3}$ M, Talerico et al., 2004 observed a moderate increase of [Nb(V)] with increasing pH. At pH ≈ 13.2 and [Ca] ≈ 10^{-4} M, the authors reported [Nb(V)] ≈ 10^{-5} M, which is in line with Nb concentrations measured in the present study at pH 13.5.

The increase in [Nb] observed at $pH_m > 12.5$ possibly reflects the formation of Nb(V) hydrolysis species beyond $Nb(OH)_7^{2-}$. Note that thermodynamic data available for the later species was derived from solubility experiments at pH ≈ 9. Above this pH, the very high solubility of β-Nb_2O_5 resulted in the formation of the secondary phase $Na_8Nb_6O_{19}$·13 H_2O(cr) and the predominance of polyniobiate species in the aqueous phase, which are not expected at the very low Nb concentrations observed in the current study. The formation of the monomeric species $NbO_2(OH)_4^{3-}$ at pH > 14.5 and [Nb] ≈ 10^{-4} M was previously proposed in the literature based on a spectrophotometric study in KOH solutions (Goiffon et al., 1973). In the presence of Ca^{2+} ions, the stabilization of such monomeric species of Nb(V) may occur at lower pH-values in the form of ternary complexes Ca–Nb(V)–OH. Note that the formation of analogous ternary complexes has been reported for other transition metals with similar oxidation state and ionic radii, e.g., Zr(IV) (Altmaier et al., 2008) and Tc(IV) (Yalçıntaş et al., 2016), with $r_{Zr^{4+}}$ 0.84 Å, $r_{Nb^{4+}}$ 0.74 Å and $r_{Tc^{4+}}$ 0.65 Å (all radii corresponding to CN 8, except for Tc with CN 6 (Shannon, 1976)). In a recent study, Yamaguchi and co-workers investigated the sorption and solubility of Nb(V) in near-neutral to alkaline solutions containing Ca (Yamaguchi et al., 2020). The authors observed a positive correlation between [Ca] and dissolved [Nb] in the solubility experiments with Nb_2O_5(s) at $7 \leq pH \leq 11$, and proposed a solid phase transformation to Ca $(NbO_3)_2$(s) and the predominance of $CaNb(OH)_6^+$ in the aqueous phase. No solid phase characterization was performed, and thus the possible formation of $Ca(NbO_3)_2$(s) remains speculative. Considering the predominance of $Nb(OH)_7^{2-}$ at pH > 9 in the absence of Ca, it appears as counterintuitive and unlikely that a ternary complex with less hydroxide groups (i.e., $CaNb(OH)_6^+$) prevails up to pH ≈ 11. In spite of these shortcomings, our experimental results provide additional support on the formation and relevance of ternary complexes Ca–Nb(V)–OH in hyperalkaline systems containing Ca, considering also the analogy with Zr(IV) or Tc(IV).

3.2. *Characterization of Nb(V) solid controlling the solubility*

3.2.1. *XRD and SEM-EDS analysis*

After terminating the solubility experiments, Nb(V) solid phases were separated from the supernatant solutions, washed and dried under Ar atmosphere. Elemental analysis conducted after dissolution of the Nb (V) revealed the presence of Ca and Nb in all solids, unambiguously confirming that Ca-Nb(V) solids were formed and controlled the Nb(V) solubility in all investigated systems (see Table SD-2 in Supplementary Data). The Ca/Nb ratio in the solid phases equilibrated at $pH_m \approx 10$ ranged between 0.5 and 0.6 and was mostly independent of the Ca concentration in aqueous phase. A trend to increase the Ca/Nb ratio in the solid phase with increasing Ca concentration in aqueous phase was observed at $pH_m \approx 11$ and 12, thus reflecting a more hydrolyzed environment of Nb in the solid phase with increasing pH. The solid phase equilibrated at $pH_m \approx 12$ and the highest Ca aqueous concentration ([Ca] 3×10^{-2} M) shows a Ca/Nb ratio of ≈ 1, as quantified both by quantitative chemical analysis and SEM-EDS. The same Ca/Nb ratio was determined for the solid equilibrated in the pore water solution with [Ca] 1.4×10^{-3} M. Besides Ca, the incorporation of K was also identified in the Nb solid phases equilibrated in the two investigated pore water solutions, whereas no Na was observed in any of the solid phases in spite of the high NaOH concentration present in pore water.

Fig. 2 displays the XRD patterns of Ca–Nb(V) solid phases collected from the oversaturation solubility experiments. Diffraction patterns of solid phases equilibrated in pore water match well reference peaks reported for the $Ca_2Nb_2O_7$(cr) cubic pyrochlore structure (PDF file 81–0841, marked as *P* in Fig. 2). This assignment is in line with the stoichiometry Ca/Nb ≈ 1 determined for the sample equilibrated in pore water with [Ca] 1.4×10^{-3} M. Besides the main features of $Ca_2Nb_2O_7$(cr) cubic pyrochlore, distinct sharp peaks at 2θ 22.0 and 31.6 are observed for the sample equilibrated in pore water with lower calcium concentration, i.e., [Ca] 3.5×10^{-4} M. These patterns suggest the presence of $KNbO_3$ (PDF 32–0822, indicated as *K* in Fig. 2), consistently with the higher potassium content determined for this solid phase by quantitative chemical analysis (see Table SD-2 in Supplementary Data). The solid phase equilibrated at $pH_m \approx 12$ and [Ca] 3×10^{-2} M shows broad diffraction patterns consistent with the $Ca_2Nb_2O_7$(cr) cubic pyrochlore structure, in excellent agreement with a Ca/Nb ratio of ≈ 1 determined for this solid phase by quantitative chemical analysis and SEM-EDS. Sharper and intricate features are obtained for the rest of the samples at $pH_m \approx 12$ with lower aqueous Ca concentrations, which reflect a more crystalline character and possible co-existence of several Nb solid phases. A split of the main reflection at 2θ 29.4° and 29.7° is observed for these samples, which can be assigned to orthorhombic $CaNb_2O_6$(cr) (PDF 39–1392) and cubic pyrochlore $Ca_2Nb_2O_7$(cr), respectively. The relative intensity of both peaks shows a good qualitative agreement with the Ca/Nb ratio determined for the corresponding solid phases, as shown in Figure SD-1 and Table SD-2 in the Supplementary Data. Other solid phases beyond $CaNb_2O_6$(cr) and $Ca_2Nb_2O_7$(cr) are possibly present in this complex system, although no unequivocal assignment can be done on the basis of the available

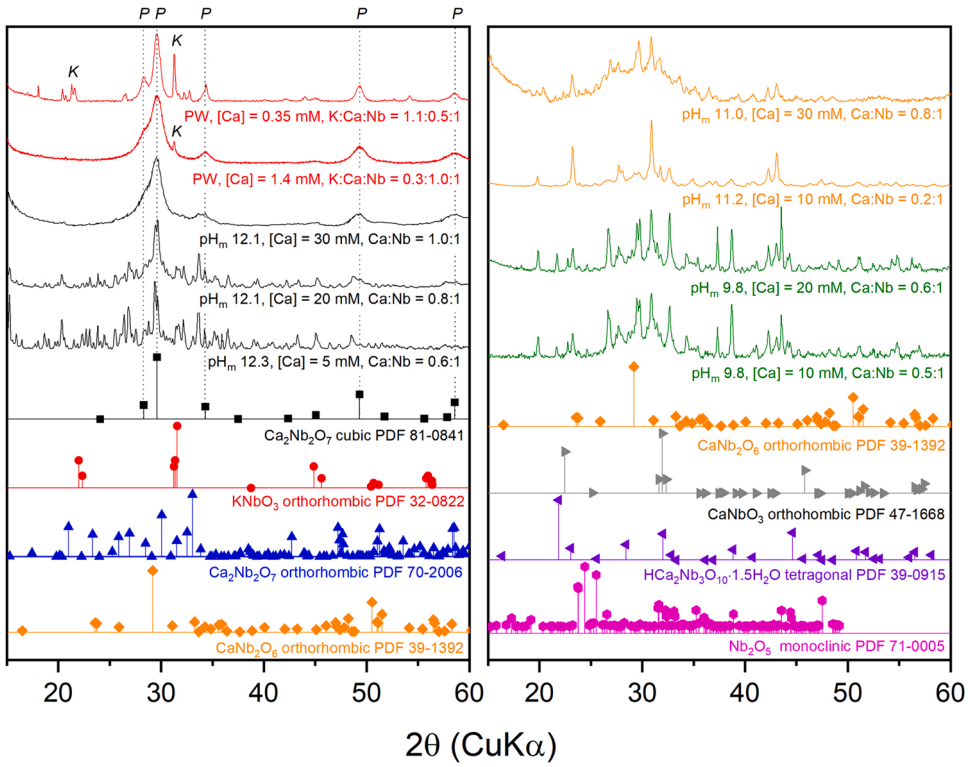

Fig. 2. Representative X-ray diffraction patterns of Ca–Nb(V) solids with experimental condition (pH_m and initial [Ca]) and the stoichiometry of (K:)Ca:Nb. The patterns of PW at [Ca] = 1.4 mM were obtained from (Çevirim-Papaioannou et al., 2022). Reference peaks of Nb(V) solids were given for the comparison. P: $Ca_2Nb_2O_7$ cubic pyrochlore Powder Diffraction File (PDF) 81–0841 and K: $KNbO_3$ PDF 32–0822.

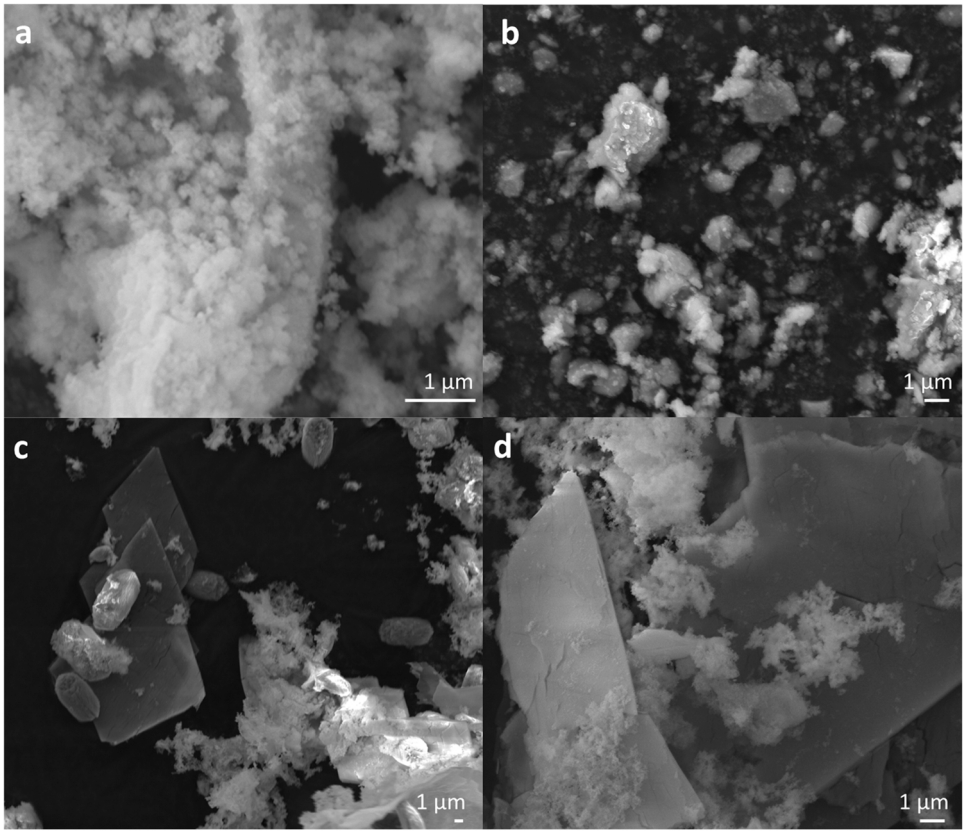

Fig. 3. Scanning electron microscopic images collected from Ca-Nb(V) solids phases equilibrated in a) cementitious pore water with $pH_m \approx 13.5$ and [Ca] $= 1.4 \times 10^{-3}$ M; b) $pH_m \approx 12.1$ and [Ca] $= 3.0 \times 10^{-2}$ M; c) $pH_m \approx 11.0$ and [Ca] $= 3.0 \times 10^{-2}$ M; d) $pH_m \approx 10$ and [Ca] $= 2.0 \times 10^{-2}$ M. The predominance of pyrochlore in Samples a and b was confirmed by XRD analysis.

diffractograms. However, the presence of orthorhombic (PDF 70–2006) and monoclinic (PDF 74–0390, not shown in Fig. 2 due to very similar diffraction with PDF 70–2006) $Ca_2Nb_2O_7$(cr) can be speculated based on the similarity in the scattered patterns and Ca/Nb ratio. XRD patterns of samples equilibrated at $pH_m \approx 10$ and 11 support a more predominant role of the orthorhombic $CaNb_2O_6$(cr) (columbite, see peak at 2θ 29.3°), in line with the generally lower Ca/Nb ratio quantified for these samples. Other patterns in these diffractograms could be tentatively assigned to $CaNbO_3$(cr) (PDF 47–1668), $HCa_2Nb_3O_{10}{\cdot}1.5\ H_2O$(cr) (PDF 39–0915), or Nb_2O_5(cr) (PDF 71–0005).

Fig. 3 shows representative SEM images of the investigated Ca-Nb(V) solid phases. Fig. 3a and b correspond to the pyrochlore-dominated samples equilibrated in pore water with [Ca] 1.4×10^{-3} M and at $pH_m \approx 12$ with [Ca] 3.0×10^{-2} M, respectively. The nanostructured material observed in both figures is consistent with the broad XRD patterns shown for these samples in Fig. 2, and is in line with previous observations reported for cubic pyrochlore (Cho et al., 2010; Nakamura et al., 2015). SEM images collected for samples equilibrated at $pH_m \approx 11$ and 10 (Fig. 3c and d) reflect also the diversity in morphology highlighted by XRD. In addition to the nanostructured particles, solid phases with platelet- and ellipsoid-like morphologies are observed in these samples, which resemble previously reported SEM images of $CaNb_2O_6$(cr) (Cho et al., 2010) and $HCa_2Nb_3O_{10}$(cr) (Chen et al., 2008). Ca/Nb ratios determined by EDS are consistent with results obtained by quantitative chemical analysis (Table SD-2 in Supplementary Data).

3.2.2. *Raman spectroscopy*

Fig. 4a shows the Raman mapping collected for the surface (100 × 100 μm) of the solid phase equilibrated in cementitious pore water with $pH_m \approx 13.5$ and [Ca] 1.4×10^{-3} M. Raman data unequivocally confirm the predominance of cubic pyrochlore $Ca_2Nb_2O_7$(cr) for this sample, with its characteristic bands at 640 cm^{-1} and 810 cm^{-1} (Fig. 4b) (Zietlow et al., 2017; Reissner et al., 2020). The broad Raman bands reflect the low crystallinity and/or structural disorder of the pyrochlore structure. These observations are in excellent agreement with XRD, SEM-EDS and quantitative chemical analysis of this solid phase. The additional Raman bands observed at ≈ 2800–2950 cm^{-1} belong to C-H stretching modes and can be attributed to organic impurities resulting from the washing of the solid phase with ethanol. Raman confirms also the predominance of the cubic pyrochlore structure in the solid phases equilibrated in cementitious pore water with low Ca content ($pH_m \approx$ 13.5, [Ca] 3.5×10^{-4} M) as well as at $pH_m \approx 12$ with high Ca content ([Ca] 3.0×10^{-2} M) (see Figures SD-2 and SD-3 in the Supplementary Data), whilst two additional Raman bands at 841 cm^{-1} and ≈ 900 cm^{-1} are also observed in both cases. No Raman features corresponding to cubic pyrochlore are observed in the solid phases with low Ca/Nb ratios forming at $pH_m \approx 10$, 11, and 12, whereas signals at 841 cm^{-1} and ≈ 900 cm^{-1} were repeatedly observed in the phase distribution diagrams (see Figures SD-4 and 5 in Supplementary Data).

Fig. 5 shows the Raman analysis with frequency assignment of the Ca–Nb(V) solids identified. The pyrochlore structure with ideal formula $A_2B_2O_7$ crystallizes in space group $Fd\bar{3}m$ and could be considered an anion-deficient derivative of the fluorite structure (AO_2). Main features are the corner-sharing BO_6 octahedra and A_2O chains (Chakoumakos, 1984; Glerup et al., 2001). The factor group analysis of the cubic pyrochlore structure reveals six Raman-active modes which involve the motion of oxygen atoms (McCauley, 1973; Arenas et al., 2010). The low-frequency modes of cubic pyrochlore have been assigned to the splitting of F_{2g} mode of A–O and B–O (Arenas et al., 2010; Hong et al., 2003). Accordingly, the bands of cubic pyrochlore obtained from the solid equilibrated in cementitious pore water (Fig. 5a) at 112 and 182 cm^{-1} could be explained by Nb–O and Ca–O stretching, respectively. On the other hand, Arenas et al. suggested that the low-frequency modes could be indicative of a IR active F_{1u} mode caused by the relaxation of the selection rules due to the displacement disorder of the A site (Arenas et al., 2010). Broad bands from 200 to 500 cm^{-1} were attributed to F_{2g} and E_g modes (Arenas et al., 2010; Hong et al., 2003; Vandenborre and Husson, 1984). The strong signal centered at 641 cm^{-1} with a pronounced shoulder at 545 cm^{-1} could be ascribed to F_{2g} and A_{1g} modes due to bending of O–Nb–O (Arenas et al., 2010) or Nb–O modes (Vandenborre and Husson, 1984). The assignment of the 809 cm^{-1} signal is uncertain, but could be associated with a forbidden mode due to the relaxation of the selection rules (Zietlow et al., 2017; Arenas et al., 2010). Hong et al., 2003 proposed that the band observed at 768 cm^{-1} in the Raman spectra of $Bi_{1.5}ZnNb_{1.5}O_7$ pyrochlores could respond to A_{1g} mode of Nb–O stretching. Otherwise, a possibility of combination bands could be suggested (Vandenborre and Husson, 1984). The minor band at 1078 cm^{-1} is typical ν_1-CO_3 mode, reflecting the presence of a minor impurity of calcite.

Li et al., 2017 investigated solid solutions of Ba in $Ca_2Nb_2O_7$(cr) using XRD and Raman analysis. The XRD pattern of $Ca_2Nb_2O_7$(cr) was indexed to a space group $P2_1$ (i.e., monoclinic perovskites-like layered structure), whereas the presence of $CaNb_2O_6$(cr) as a secondary phase was identified in the $Ca_{2-x}Ba_xNb_2O_7$ systems with $x \geq 0.4$. The authors assigned also the strong peak at 841 cm^{-1} to monoclinic $Ca_2Nb_2O_7$(cr), which matches well the main Raman feature observed in the sample of cementitious pore water with [Ca] 3.5×10^{-4} M as well as the solid equilibrated at $pH_m \approx 12$ with [Ca] 3.0×10^{-2} M (see Fig. 5b). The

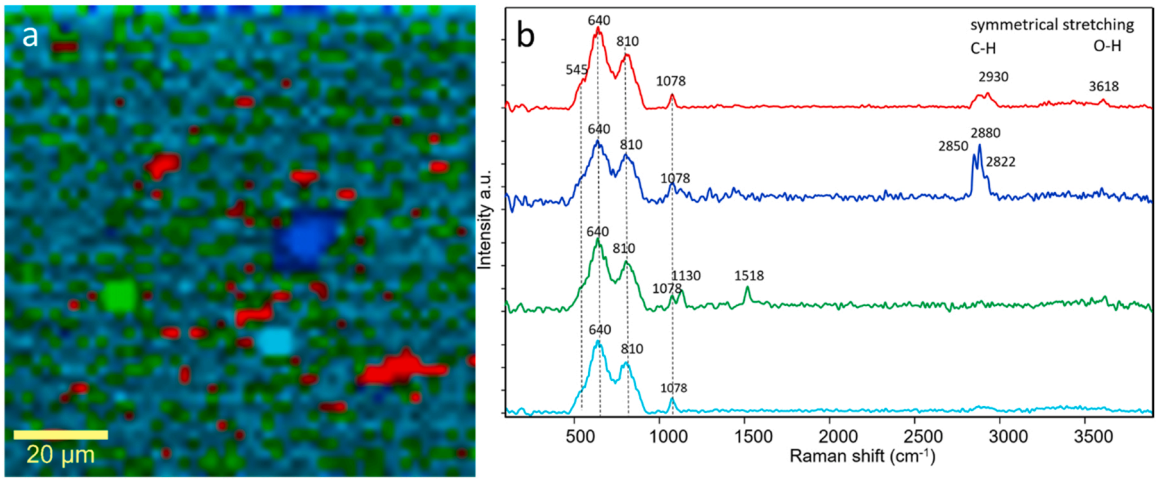

Fig. 4. (a) Phase distribution obtained by Raman mapping of the solid sample equilibrated in cementitious pore water with $pH_m \approx 13.5$ and [Ca] = 1.4×10^{-3} M. (b) Raman spectra of the single components identified in figure (a), showing the predominance of cubic pyrochlore. Dashed lines indicate the main Raman bands of cubic pyrochlore as reported in (Zietlow et al., 2017; Reissner et al., 2020) (see also text).

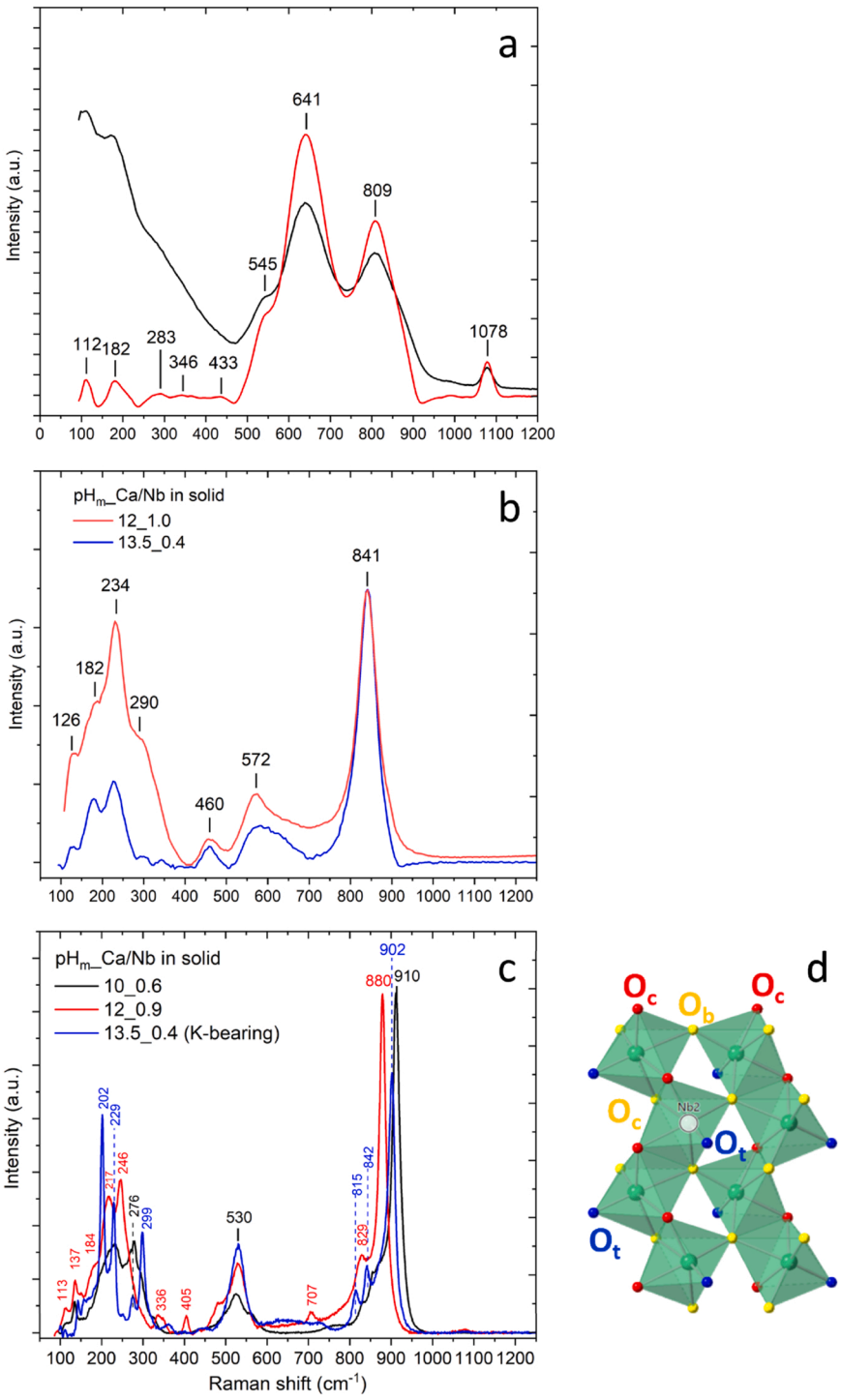

Fig. 5. Raman signals with frequency assignment: (a) raw and background-subtracted signal of cubic pyrochlore (solid equilibrated in cementitious pore water with Ca/Nb ≈ 1, identical sample as in Fig. 4); (b) Signal with the main peak at 841 cm ^{1} attributed to orthorhombic or/and monoclinic $Ca_2Nb_2O_7$; (c) Signal with the main peak at ≈ 900 cm ^{1} assigned to columbite (d) Scheme of the Nb–O chain in the columbite structure. The sample with Ca/Nb = 0.4 at pH 13.5 shows different Raman features (b and c) depending on the investigated site. See text for detailed frequency assignments.

main peak at 841 cm^{-1} possibly reflects the structural transformation of cubic pyrochlore to orthorhombic and/or monoclinic $Ca_2Nb_2O_7$(cr), and can be attributed to Nb–O stretching mode, with the corresponding bending modes being centered at 460 cm^{-1} and 572 cm^{-1} (Li et al., 2017).

The Raman signal at ≈ 900 cm^{-1} frequently recorded in the solid phases equilibrated at pH$_m$ ≈ 10 and 11 with low Ca content (Fig. 5c) can be assigned to columbite, $CaNb_2O_6$(cr) (Husson et al., 1977; Mathai et al., 2014; Pena et al., 2020). In columbite with a space group *Pbcn* (orthorhombic), Ca^{2+} and Nb^{5+} are six-fold coordinated, whereas three kinds of non-equivalent O^{2-} sites are available (O_b, O_c and O_t, see Fig. 5d). The bridging oxygen (O_b site) is bonded to three equivalent Nb atoms. The oxygen O_c (chain site) connects one Ca and two Nb atoms, while the oxygen O_t located at "terminal site" associates with two Ca and one Nb atoms. Ca and Nb octahedra form a zigzag edge-sharing chains along the c-axis (Cummings and Simonsen, 1970). As shown in Fig. 5c, the Raman spectrum illustrates an intensive peak at ≈ 900 cm^{-1} assigned to the A_g symmetry of Nb–O_t bonds in columbite (Husson et al., 1977; Mathai et al., 2014; Pena et al., 2020). The spectral position is likely affected by the Ca content in the solid and the neighboring atom of O_t. The frequency of Nb–O_t located at 880 cm^{-1} and 910 cm^{-1} for the solids with relatively high (Ca/Nb 0.86) and low (Ca/Nb 0.62) Ca contents, respectively, can be correlated to the neighboring environment adjacent to O_t (namely, Ca–O_t or H–O_t bonds). The Ca-Nb(V) solid with

high K content (K:Ca:Nb 1:0.3:1) showed the frequency at 902 cm^{-1} assigned to K–O_t bond. The signal from 380 cm^{-1} to 800 cm^{-1} may correspond to stretching modes of O_b in NbO_6 octahedra, while the low frequency at < 380 cm^{-1} seems the bending and torsion modes of O–Nb–O (Pena et al., 2020).

Raman analysis unambiguously confirmed the presence of H_2O in most of the investigated Ca-Nb(V) solid phases, as observed with the characteristic broad band at 3000–3700 cm^{-1}. The release of water observed at $T > 100$ ℃ in the TG analysis provided indirect evidence on the possible presence of water in the structure of the Ca-Nb(V) solid phases (Figure SD-6 in Supplementary Data). The presence of water in the crystal structure is expected to contribute to the diversity of Ca—Nb(V) oxides observed within this work.

4. Summary and conclusions

A detailed investigation on the solubility of Nb(V) was conducted in alkaline to hyperalkaline solutions containing Ca, which are representative of cementitious environments foreseen in several repository concepts for the disposal of L/ILW. Solid phases forming under these conditions were characterized using a multi-method approach, including XRD, SEM-EDS, Raman spectroscopy, TG and quantitative chemical analysis.

In contrast to the very high solubility of Nb(V) in alkaline NaCl–NaOH solutions, the presence Ca in concentrations as low as 3.5×10^{-4} M triggers a very significant drop in the niobium concentration to [Nb(V)] $\approx 10^{-9}$–10^{-6} M, depending upon pH and [Ca]. These observations cannot be explained with thermodynamic data available for Nb_2O_5(s) or Na–Nb(V)–O/OH(s) solid phases, and thus provide evidence on the formation of sparingly soluble Ca–Nb(V)–O/OH(s) compounds. A solubility minimum with [Nb(V)] $\approx 10^{-9}$ M is obtained at pH $\approx$ 12–12.5 for all investigated Ca concentrations, whereas niobium concentration increases up to $\approx 10^{-6}$ M at pH $\approx$ 13.5. This observation can be explained by the formation at $pH > 12$ of higher hydrolysis species beyond $Nb(OH)_7^{2-}$, possibly as condensed moieties such as $NbO_2(OH)_4^{3-}$. Based on the analogy with other transition metals of similar charge and ionic radii, e.g., Zr(IV), Tc(IV), we speculate that the formation of such highly charged species is further stabilized by the complexation with Ca.

Quantitative chemical analysis of the precipitates collected from the solubility experiments systematically confirm the stoichiometric presence of Ca in the solid phases controlling the solubility of niobium. A larger fraction of Ca is observed in the solid phases equilibrated at pH $\approx$ 12 – 13.5 (with Ca/Nb ratio $\approx$ 1), whereas a Ca/Nb ratio $\approx$ 0.5 was quantified pH $\approx$ 10 – 11. In cement pore water containing high K (0.37 M) and low Ca concentration (3.5×10^{-4} M), a significant substitution of Ca by K was also observed. In contrast to K, Na is not incorporated in the structure of the solid, in spite of the relatively high Na concentration in the cement pore water (0.14 M).

XRD analyses support that cubic pyrochlore, $Ca_2Nb_2O_7$(cr), is the main solid phase in cement pore water with pH $\approx$ 13.5 and [Ca] $\approx 1.4 \times 10^{-3}$ M. At the same pH but lower [Ca], the incorporation of K in the cubic pyrochlore structure was identified on the basis of the sharp diffraction peak at 2θ 31.6°, in line with results obtained from quantitative chemical analysis. XRD confirmed also the cubic pyrochlore structure for the solid phase with Ca/Nb ratio $\approx$ 1 equilibrated at pH $\approx$ 12. At the same pH but for samples with lower Ca/Nb ratio, the presence of orthorhombic / monoclinic $Ca_2Nb_2O_7$(cr) and orthorhombic $CaNbO_6$ is proposed based on the main diffraction features. XRD patterns of samples equilibrated at $pH_m \approx 10$ and 11 support a more predominant role of the orthorhombic $CaNb_2O_6$(cr), in line with the generally lower Ca/Nb ratio quantified for these samples. However, the intricate powder pattern supports the co-existence of other solid phases and / or crystal structures in these conditions.

Phase distribution of the Nb(V) solid equilibrated in cement pore water (pH $\approx$ 13.5, [Ca] $\approx 1.4 \times 10^{-3}$ M) obtained by Raman mapping revealed the only presence of cubic pyrochlore $Ca_2Nb_2O_7$(cr), which is characterized by Raman signals at 641 cm^{-1} and 809 cm^{-1}. Consistently with XRD, Raman supports the structural alternation from cubic to orthorhombic / monoclinic $Ca_2Nb_2O_7$(cr) in the solids with Ca/Nb ratio < 1. The frequency at $\approx$ 900 cm^{-1} was attributed to Nb–O_t bond in orthorhombic $CaNb_2O_6$(cr), which is predominantly observed for the solid samples equilibrated at pH $\approx$ 10 and 11.

This work provides a detailed description of Nb(V) solid phase formation and solubility phenomena in cementitious systems relevant for the disposal of L/ILW. The results provide relevant inputs for the estimation of the source term of niobium in these systems, i.e., the upper solubility concentration limits that can be attained in the cement pore water. The identification of the solid phases controlling the solubility of Nb in these conditions represents an important step towards the full thermodynamic description of niobium in alkaline to hyperalkaline systems containing Ca, including both solid phases and aqueous speciation at trace niobium concentrations.

CRediT authorship contribution statement

Yongheum Jo: Methodology, Investigation (sample preparation, solubility experiments, and XRD), Writing – original draft, Writing – review & editing. **Krassimir Garbev**: Investigation (Raman and XRD), Writing – original draft, Writing – review & editing. **Neşe Çevirim-Papaioannou:** Methodology, Investigation (sample preparation, solubility experiments). **Oliver Dieste Blanco**: Investigation (SEM), Writing – review & editing. **Benny de Blochouse:** Conceptualization, Project administration, Writing – review & editing. **Marcus Altmaier**: Conceptualization, Project administration, Funding acquisition, Writing – review & editing. **Xavier Gaona**: Conceptualization, Supervision, Project administration, Funding acquisition, Writing – original draft, Writing – review & editing.

Environmental Implications

The long-lived radioactive isotope ^{94}Nb is produced by neutron activation of stable ^{93}Nb present in structural components of nuclear reactors. ^{94}Nb is a relevant dose-contributor in repositories for low- and intermediate-level waste.

This work provides important input for estimating the source term of Nb(V) in cement-based repositories, i.e., the determination of upper concentration limits dissolved in the pore water. Solid phases controlling Nb solubility are identified under various conditions expected in the repository. This represents a key milestone towards the development of thermodynamic models that can be implemented in geochemical calculations predicting the behavior of Nb in underground repositories.

Declaration of Competing Interest

The authors declare that they have no known competing financial interests or personal relationships that could have appeared to influence the work reported in this paper.

Data availability

Data will be made available on request.

Acknowledgements

This work was partly funded by ONDRAF/NIRAS, Belgium. Frank Geyer, Annika Kaufmann and Melanie Bottle (all KIT–INE) are gratefully acknowledged for the ICP–MS/OES measurements and technical support.

References

Adams, P., Carboneau, M.L., 1995, National Low-Level Waste Management Program radionuclide report series. Volume 11, Niobium-94, DOE/LLW-127, Idaho National Engineering Laboratory, Idaho, United States of America, in, Lockheed Idaho Technologies Co.

Altmaier, M., Neck, V., Fanghanel, T., 2008. Solubility of Zr(IV), Th(IV) and Pu(IV) hydrous oxides in CaCl2 solutions and the formation of ternary Ca-M(IV)-OH complexes. Radiochim. Acta 96, 541–550.

Arenas, D.J., Gasparov, L.V., Qiu, W., Nino, J.C., Patterson, C.H., Tanner, D.B., 2010. Raman study of phonon modes in bismuth pyrochlores. Phys. Rev. B 82, 214302.

Brandon, J.K., Megaw, H.D., 1970. On the crystal structure and properties of $Ca_2Nb_2O_7$, "calcium pyroniobate". Philos. Mag.: A J. Theor. Exp. Appl. Phys. 21, 189–194.

Bube, C., Metz, V., Bohnert, E., Garbev, K., Schild, D., Kienzler, B., 2013. Long-term cement corrosion in chloride-rich solutions relevant to radioactive waste disposal in rock salt – Leaching experiments and thermodynamic simulations. Phys. Chem. Earth, Parts A/B/C. 64, 87–94.

Cachoir, C., Canniere, P.D., Druyts, F., Ferrand, K., Kursten, B., Lemmens, K., Mennecart, T., Valcke, E., 2006, Preparation of Evolved Cement Water (ECW) and Young Cement Waters (YCW and YCWCa) for the Supercontainer experiments, IW. W&D.0088, 1–9.

Çevirim-Papaioannou, N., Jo, Y., Franke, K., Fuss, M., de Blochouse, B., Altmaier, M., Gaona, X., 2022. Uptake of niobium by cement systems relevant for nuclear waste disposal: Impact of ISA and chloride. Cem. Concr. Res. 153, 106690.

Chakoumakos, B.C., 1984. Systematics of the pyrochlore structure type, ideal $A_2B_2X_6Y$. J. Solid State Chem. 53, 120–129.

Chen, Y., Zhao, X., Ma, H., Ma, S., Huang, G., Makita, Y., Bai, X., Yang, X., 2008. Structure and dehydration of layered perovskite niobate with bilayer hydrates prepared by exfoliation/self-assembly process. J. Solid State Chem. 181, 1684–1694.

Cho, I.-S., Kim, D.W., Cho, C.M., An, J.-S., Roh, H.-S., Hong, K.S., 2010. Synthesis, characterization and photocatalytic properties of $CaNb_2O_6$ with ellipsoid-like plate morphology. Solid State Sci. 12, 982–988.

Collier, J.P., Wong, S.H., Tien, J.K., Phillips, J.C., 1988. The effect of varying AI, Ti,and Nb content on the phase stability of INCONEL 718. Metall. Trans. A 19, 1657–1666.

Cummings, J.P., Simonsen, S.H., 1970. The crystal structure of calcium niobate ($CaNb_2O_6$). Am. Mineral. 55, 90–97.

Deblonde, G.J.P., Chagnes, A., Bélair, S., Cote, G., 2015a. Solubility of niobium(V) and tantalum(V) under mild alkaline conditions. Hydrometallurgy 156, 99–106.

Deblonde, G.J.P., Moncomble, A., Cote, G., Bélair, S., Chagnes, A., 2015b. Experimental and computational exploration of the UV–visible properties of hexaniobate and hexatantalate ions. RSC Adv. 5, 7619–7627.

Espartero, A.G., Suárez, J.A., Rodrıguez, M., 1998. Determination of ^{93m}Nb and ^{94m}Nb in medium and low level radioactive wastes. Appl. Radiat. Isot. 49, 1277–1282.

Gasik, M.I., 2013. Technology of niobium ferroalloys. In: Gasik, M. (Ed.), Handbook of Ferroalloys. Butterworth-Heinemann, Oxford, pp. 411–419.

Glerup, M., Nielsen, O.F., Poulsen, F.W., 2001. The structural transformation from the pyrochlore structure, $A_2B_2O_7$, to the fluorite structure, AO_2, studied by Raman spectroscopy and defect chemistry modeling. J. Solid State Chem. 160, 25–32.

Goiffon, A., Granger, R., Bockel, C., Spinner, B., 1973. Investigation of equilibria in niobium-V alkaline solutions. Rev. De. Chim. Minérale 10, 487–502.

Grivé, M., Duro, L., Colàs, E., Giffaut, E., 2015. Thermodynamic data selection applied to radionuclides and chemotoxic elements: An overview of the ThermoChimie-TDB. Appl. Geochem. 55, 85–94.

He, G.Z., Jiang, S., Zhou, Z.Y., He, M., Tian, W.Z., Zhang, J.L., Diao, L.J., Li, H., 2012. Precise half-life measurement for the ground state of 94Nb. Phys. Rev. C. 86, 014605.

Hong, W., Huiling, D., Xi, Y., 2003. Structural study of Bi_2O_3-ZnO-Nb_2O_5 based pyrochlores. Mater. Sci. Eng.: B 99, 20–24.

Husson, E., Repelin, Y., Dao, N.Q., Brusset, H., 1977. Normal coordinate analysis for $CaNb_2O_6$ of columbite structure. J. Chem. Phys. 66, 5173–5180.

Lafuente, B., Downs, R.T., Yang, H., Stone, N., 2015. 1. The power of databases: The RRUFF project. In: Thomas, A., Rosa Micaela, D. (Eds.), Highlights in Mineralogical Crystallography. De Gruyter, pp. 1–30.

Li, B., Gu, M., Nie, Z., Wei, X., Wang, C., Sprenkle, V., Wang, W., 2014. Nanorod niobium oxide as powerful catalysts for an all vanadium redox flow battery. Nano Lett. 14, 158–165.

Li, C., Xiang, H., Qin, Y., Fang, L., 2017. Effects of barium substitution on the sintering behavior, dielectric properties of $Ca_2Nb_2O_7$ ferroelectric ceramics. J. Adv. Dielectr. 07, 1750013.

Lothenbach, B., Ochs, M., Hager, D., 1999, Confinement of radioactive waste in cementitious barriers for surface and deep geological disposal, C RP 0BMG, in, Andra.

Mathai, K.C., Vidya, S., John, A., Solomon, S., Thomas, J.K., 2014. Structural, optical, and compactness characteristics of nanocrystalline $CaNb_2O_6$ synthesized through an autoigniting combustion method. Adv. Condens. Matter Phys. 2014, 735878.

McCauley, R.A., 1973. Infrared-absorption characteristics of the pyrochlore structure*. J. Opt. Soc. Am. 63, 721–725.

Nakamura, A., Tomita, O., Higashi, M., Hosokawa, S., Tanaka, T., Abe, R., 2015. Solvothermal synthesis of $Ca_2Nb_2O_7$ fine particles and their high activity for photocatalytic water splitting into H_2 and O_2 under UV light irradiation. Chem. Lett. 44, 1001–1003.

Nyman, M., 2011. Polyoxoniobate chemistry in the 21st century. Dalton Trans. 40, 8049–8058.

Peiffert, C., Nguyen-Trung, C., Landais, P., 1997, Etude experimentale de la solubilite des oxydes de Nb(V) cristallise et amorphe dans des solutions aqueuses, ANDRA report, C RP 0CRE 97–003.

Peiffert, C., Nguyen-Trung, C., Palmer, D.A., Laval, J.P., Giffaut, E., 2010. Solubility of B-Nb_2O_5 and the hydrolysis of niobium(V) in aqueous solution as a function of temperature and ionic strength. J. Solut. Chem. 39, 197–218.

Pena, J.P., Bouvier, P., Isnard, O., 2020. Structural properties and Raman spectra of columbite-type $NiNb_{2-x}V_xO_6$ synthesized under high pressure. J. Solid State Chem. 291, 121607.

N.J. Pilkington, N.S. Stone, 1990, The solubility and sorption of nickel and niobium under high pH conditions, in, United Kingdom, pp. 41.

Pointeau, I., Landesman, C., Coreau, N., Moisan, N., Reiller, P., 2004, Etude de la retention chimique des radionucleides Cs(I), Am(III), Zr(IV), Pu(IV), Nb(V), U(VI), Tc(IV) par les matérriaux cimentaires degradérs, in: CEA/DEN/SAC Report RT DPC/SECR 03–037.

Reissner, C.E., Roddatis, V., Bismayer, U., Schreiber, A., Pollmann, H., Beirau, T., 2020. Mechanical and structural response of radiation-damaged pyrochlore to thermal annealing. Materialia 14, 100950.

Schulz, K.J., Piatak, N.M., Papp, J.F., 2017, Niobium and tantalum, in: K.J. Schulz, J.J.H. DeYoung, R.R. Seal Ii, D.C. Bradley (Eds.) Professional Paper, Reston, VA, pp. 46.

Schuman, R.P., Goris, P., 1959. Half-life and decay of niobium-94. J. Inorg. Nucl. Chem. 12, 1–5.

Shannon, R.D., 1976. Revised effective ionic radii and systematic studies of interatomic distances in halides and chalcogenides, Acta crystallographica section A: crystal physics, diffraction. Theor. Gen. Crystallogr. 32, 751–767.

Tachi, Y., Suyama, T., Mihara, M., 2020, Data acquisition for radionuclide sorption on barrier materials for performance assesement of geological disposal of TRU wastes, JAEA-Data/Code 2019–021.

Talerico, C., Ochs, M., Giffaut, E., 2004, Solubility of niobium(V) under cementitious conditions: importance of Ca-niobate, MRS Online Proceedings Library, 824, 414–419.

Vandenborre, M.T., Husson, E., 1984. Comparison of the force field in various pyrochlore families. II. Phases presenting structural defects. J. Solid State Chem. 53, 253–259.

Wang, L., Martens, E., Jacques, D., Canniere, P.D., Mallants, D., Berry, J., 2009, Review of sorption values for the cementitious near field of a near surface radioactive waste disposal facility, in: Project Near Surface Disposal of Category A Waste at Dessel, ONDRAF/NIRAS Technical Report, NIROND-TR Report 2008–23E, NIRAS-MP5–03 DATA-LT(NF), Version 1, Brussels, Belgium.

Yalçıntaş, E., Gaona, X., Altmaier, M., Dardenne, K., Polly, R., Geckeis, H., 2016. Thermodynamic description of Tc(iv) solubility and hydrolysis in dilute to concentrated NaCl, MgCl2 and CaCl2 solutions. Dalton Trans. 45, 8916–8936.

Yamaguchi, T., Ohira, S., Hemmi, K., Barr, L., Shimada, A., Maeda, T., Iida, Y., 2020. Consideration on modeling of Nb sorption onto clay minerals. Radiochim. Acta 108, 873–877.

Zhang, X., Peng, N., Liu, T., Zheng, R., Xia, M., Yu, H., Chen, S., Shui, M., Shu, J., 2019. Review on niobium-based chalcogenides for electrochemical energy storage devices: Application and progress. Nano Energy 65, 104049.

Zhou, C., Shi, R., Waterhouse, G.I.N., Zhang, T., 2020. Recent advances in niobium-based semiconductors for solar hydrogen production. Coord. Chem. Rev. 419, 213399.

Zietlow, P., Beirau, T., Mihailova, B., Groat, L.A., Chudy, T., Shelyug, A., Navrotsky, A., Ewing, R.C., Schlüter, J., Škoda, R., Bismayer, U., 2017. Thermal annealing of natural, radiation-damaged pyrochlore. Zeitschrift für Kristallographie - Crystalline Mater. 232, 25–38.